JACS
JOURNAL OF THE AMERICAN CHEMICAL SOCIETY

ARTICLE

pubs.acs.org/JACS

Solution-Deposited Organic–Inorganic Hybrid Multilayer Gate Dielectrics. Design, Synthesis, Microstructures, and Electrical Properties with Thin-Film Transistors

Young-geun Ha,[†] Jonathan D. Emery,[‡] Michael J. Bedzyk,[‡,§] Hakan Usta,[∥] Antonio Facchetti,*[,†,∥] and Tobin J. Marks*[,†,‡]

[†]Department of Chemistry, [‡]Department of Materials Science and Engineering, and the Materials Research Center, and [§]Department of Physics and Astronomy, Northwestern University, 2145 Sheridan Road, Evanston, Illinois 60208, United States

[∥]Polyera Corporation, 8045 Lamon Avenue, Skokie, Illinois 60077, United States

Supporting Information

ABSTRACT: We report here on the rational synthesis, processing, and dielectric properties of novel layer-by-layer organic/inorganic hybrid multilayer dielectric films enabled by polarizable π-electron phosphonic acid building blocks and ultrathin ZrO_2 layers. These new zirconia-based self-assembled nanodielectric (Zr-SAND) films (5−12 nm thick) are readily fabricated via solution processes under ambient atmosphere. Attractive Zr-SAND properties include amenability to accurate control of film thickness, large-area uniformity, well-defined nanostructure, exceptionally large electrical capacitance (up to 750 nF/cm^2), excellent insulating properties (leakage current densities as low as 10^{-7} A/cm^2), and excellent thermal stability. Thin-film transistors (TFTs) fabricated with pentacene and PDIF-CN_2 as representative organic semiconductors and zinc−tin−oxide (Zn−Sn−O) as a representative inorganic semiconductor function well at low voltages (<±4.0 V). Furthermore, the TFT performance parameters of representative organic semiconductors deposited on Zr-SAND films, functionalized on the surface with various alkylphosphonic acid self-assembled monolayers, are investigated and shown to correlate closely with the alkylphosphonic acid chain dimensions.

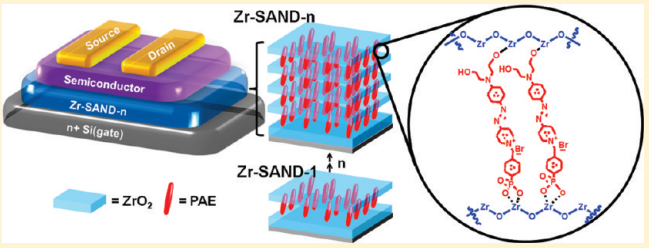

INTRODUCTION

Thin-film transistors (TFTs) fabricated from unconventional materials and by unconventional methodologies are of interest for future low-cost electronic applications such as printed RF-ID cards, flexible displays, and sensors.[1−14] Transistors are the key components used for current modulation and switching in all modern electronic devices (Figure 1). The basic working principle of TFTs is that the channel source and drain current (I_{DS}) in saturation is modulated by the source-gate bias (V_G) according to eq 1:

$$I_{DS} = \frac{W}{2L}\mu C_i(V_G - V_T)^2 \qquad (1)$$

where W/L is the channel width/length, C_i is the dielectric capacitance per unit area, μ is the charge carrier mobility, V_G is the source-gate voltage, and V_T is the threshold voltage. Depending on the charge carrier sign in the channel between source and drain, the semiconductor is either hole- (p-type) or electron-transporting (n-type). The two most important parameters governing TFT performance are the field-effect mobility (μ) and the current on/off ratio (I_{on}/I_{off}). These parameters define the drift velocity of the charge carriers in the semiconductor layer under the source/drain electric field and the current modulation between the TFT "on" and "off" states upon a gate voltage change, respectively.

Over the past two decades, solution-processable organic, inorganic, and polymeric semiconductors were developed due to attractions such as printability, the possibility of large-area depositions, low-cost device fabrication, and compatibility with mechanically flexible substrates.[15−23] Despite recent progress, one principal limitation of these semiconductors is their relatively low carrier mobilities, well below those of most silicon-based high-performance materials.[24−26] As a result, TFTs fabricated from these semiconductors require high operating voltages to attain usable drain current (I_{DS}). For low power applications such as RF-ID tags, flat panel displays, and portable electronics, it is mandatory to achieve high TFT drain currents (I_{DS}) at acceptably low operating voltages. Without changing device geometry (W and L) and semiconductor material (μ), an alternative to overcome these mobility limitations is to increase the gate dielectric capacitance C_i, given by eq 2:

$$C_i = \varepsilon_0\frac{k}{d} \qquad (2)$$

From eq 2, note that operating bias reduction can be achieved by either increasing the dielectric constant (k) or decreasing the

Received: March 27, 2011
Published: May 24, 2011

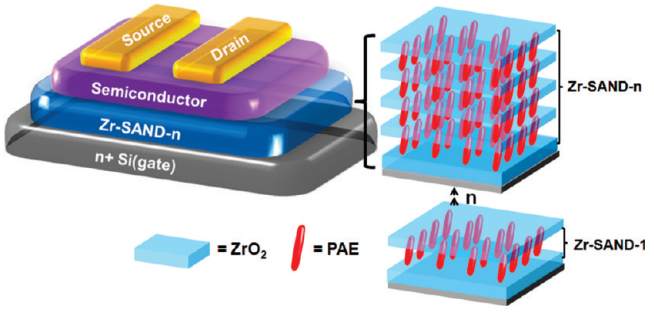

Figure 1. Schematic of a bottom-gate top-contact thin-film transistor (TFT) device geometry and the zirconia-phosphonate self-assembled nanodielectric (Zr-SAND) employed in this study.

thickness (d) of the gate dielectric layer. An attractive approach is to employ high-k materials such as metal oxide (MO) films; however, high-quality MO dielectric films typically require high growth/annealing temperatures (>400 °C) and/or expensive vacuum deposition technologies to ensure acceptably low leakage currents.[27,28] Therefore, a promising and challenging approach to lower the operating voltages is to use solution-processable high-k dielectrics fabricated at low temperature, which afford high capacitance values as well as low leakage currents.

Organic−inorganic hybrid thin films are of interest for advanced electronics applications due to the potential for combining the distinctive properties of both the organic and the inorganic components. Hybrid materials provide both the optical, electrical, and environmental durability of inorganic materials, as well as the mechanical flexibility and properties tunability of organic materials.[29,30] Several groups have reported very low operating voltage OTFTs using hybrid materials combining self-assembled monolayers (SAMs) with ultrathin MO layers such as those of HfO_x, AlO_x, and ZrO_x.[31−36] However, the SAM thicknesses of these hybrid films are limited by the singly functionalized self-assembly precursors, and it has been impossible to fabricate multilayers with well-defined growth characteristics. A key to utilizing multilayered organic−inorganic hybrid materials in unconventional TFTs and other applications is the ability to prepare high-quality multilayers in the simplest and most reliable manner. Vapor-phase fabrication methods for organic−inorganic hybrid materials are promising approaches to high-quality hybrid films;[37−39] however, they typically require high- or medium-vacuum deposition equipment (e.g., atomic layer or chemical/physical vapor deposition), and low-cost pathways for integration into large-volume coating processes are not obvious. Layer-by-layer solution-based deposition of well-defined organic precursors allows the realization of a range of functional materials with a high degree of order and structural control at the molecular level. A variety of such assemblies have been reported, often based on siloxane chemistry[40,41] or on metal−ligand coordination.[42−46] Among these materials systems, this laboratory reported a class of silane-based nanodielectrics called self-assembled nanodielectrics (SANDs) consisting of alternating organic−inorganic multilayers, chemically bound by strong siloxane linkages, and offering promising properties for a variety of opto-electronic applications, including TFTs.[47−51] However, this self-assembly approach uses ambient-sensitive and highly reactive chlorosilane reagents, which require anhydrous atmospheres and manipulation to control their chemistry. Therefore, the question arises as to whether it might

Scheme 1. Synthesis of Polarizable Phosphonic Acid-Based π-Electron Building Block

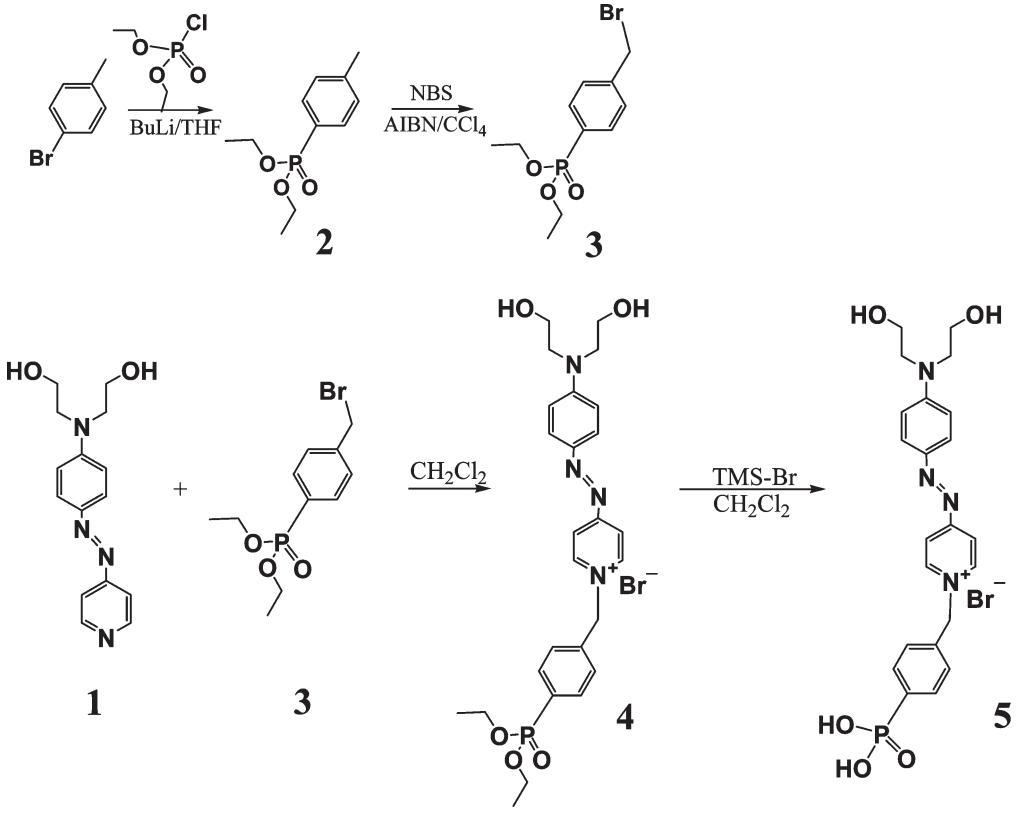

dx.doi.org/10.1021/ja202755x |J. Am. Chem. Soc. 2011, 133, 10239–10250

be possible to use alternative self-assembly strategies to fabricate high-performance multilayer gate dielectrics for TFT applications. In this contribution, we demonstrate a new approach to organic−inorganic hybrid multilayer gate dielectrics for OTFTs using polarizable, phosphonic acid-functionalized organic precursors combined with ultrathin layers of high-k inorganic oxide materials. It will be seen that these reagents are well-suited for ambient atmosphere fabrication of self-assembled multilayers, exhibiting high capacitance (465−750 nF/cm^2) and low leakage current density ($\sim$10^{-7}A/cm^2 at 2 MV/cm), grown in a simple and highly reliable manner, providing uniformly structured multilayers via a solution process. Furthermore, it will be shown that these dielectrics function effectively with both representative organic and inorganic semiconductors and can be modified by various self-assembled monolayers (SAMs) to enhance the TFT performance even further.

EXPERIMENTAL SECTION

Materials. Phosphonic acid-based π-electron (PAE) precursor **5** was straightforwardly synthesized as shown in Scheme 1. Chemical reagents for synthesis were purchased from Aldrich Chemical Co. unless otherwise indicated. The precursors for the ZrO_2 layers were prepared using zirconium(IV) chloride (99.5%, Aldrich). Heavily n-doped Si wafers (Montco Silicon Tech, Inc.) for gate electrodes were cleaned according to standard procedures. For phosphonic acid-based self-assembled monolayers (PA-SAMs), n-hexyl-phosphonic acid (PA-C6), n-dodecylphosphonic acid (PA-C12), n-tetradecylphosphonic acid (PA-C14), and n-octadecylphosphonic acid (PA-C18) were purchased from Alfa Aesar and used without further purification. Pentacene (**P5**) for the p-type organic semiconductor TFTs was commercially available and was purified by published procedures.[52] The multiple high vacuum temperature gradient sublimed perylene diimide semiconductor (**PDIF-CN$_2$**) from Polyera Corp. was chosen as the n-type organic semiconductor. The precursors for zinc tin oxide were prepared using zinc acetate dihydrate (98%, Aldrich) and tin chloride(II) (98%, Aldrich).

Synthesis of Phosphonic Acid-Based π-Electron Precursor PAE (5). *Synthesis of Diethyl p-Tolylphosphonate (**2**).* A solution of 1-bromo-4-methylbenzene (3.42 g, 20 mmol) in 140 mL of anhydrous THF was stirred at −78 °C under nitrogen, and 1 equiv of n-BuLi in hexane (1.6 M) was added. After 10 min, diethylchlorophosphate (3.45 g, 20 mmol) was added to the reaction mixture, and then stirring was continued for 1 h. After reaching room temperature, ethyl ether (100 mL) and aqueous $NaHCO_3$ ($\sim$1 g in 100 mL of H_2O) were added for extraction. The organic layer was then separated and concentrated. ^{1}H NMR (500 MHz, CD_3Cl): δ 7.70−7.74 (m, 2H), 7.28−7.30 (m, 2H), 4.06−4.15 (m, 4H), 2.42 (s, 3H), 1.31−1.34 (t, 6H).

*Synthesis of Diethyl 4-(Bromomethyl)phenylphosphonate (**3**).* A small amount of azobisisobutyronitrile (0.016 g, 0.10 mmol) was added in portions to a suspension of diethyl p-tolylphosphonate (0.73 g, 3.2 mmol) and N-bromosuccinimide (0.57 g, 3.2 mmol) in anhydrous CCl_4 (30 mL). The mixture was refluxed for 4 h, then cooled to 10 °C, and filtered to remove succinimide. The filtrate was washed with water (30 mL) and brine (30 mL) and then dried over anhydrous Na_2SO_4. After filtration, the crude product was obtained via evaporation of the solvent and was purified by chromatography on silica gel (hexene/ethyl acetate: 2/1 as eluent) to provide diethyl 4-(bromomethyl)phenylphosphonate as a colorless oil. ^{1}H NMR (500 MHz, CD_3Cl): δ 7.79−7.83 (m, 2H), 7.50−7.52 (m, 2H), 4.51 (s, 2H), 4.09−4.18 (m, 4H), 1.33−1.36 (t, 6H).

*Synthesis of 4-[[4-[Bis(2-hydroxyethyl)amino]phenyl]diazenyl]-1-(4-phosphonobenzyl) Pyridinium Bromide (**4**).* A mixture of 4-[[4-[N,N-bis(hydroxylethyl)amino]phenyl]azo]pyridine (**1**)[47] (0.286 g, 1.00 mmol) and 4-(bromomethyl)phenylphosphonate (**3**) (0.317 g, 1.00 mmol) was dissolved in CH_2Cl_2 (10 mL). The red mixture was heated under a nitrogen atmosphere at 60 °C for 4 h. The solvent was then removed under high vacuum, and the residue was dried under high vacuum overnight. ^{1}H NMR (500 MHz, DMSO-d_6): δ 9.07 (d, 2H, J_{H-H} = 6 Hz), 8.14 (d, 2H, J_{H-H} = 7 Hz), 7.90 (d, 2H, J_{H-H} = 9.5 Hz), 7.76−7.80 (m, 2H), 7.62−7.64 (m, 2H), 7.07 (d, 2H, J_{H-H} = 9.5 Hz), 5.88 (s, 2H), 4.95−4.97 (m, 2H), 3.99−4.03 (m, 4H), 3.99−4.03 (m, 4H), 3.66−3.72 (m, 8H), 1.22 (t, 3H). ^{31}P NMR (400 MHz, DMSO-d_6): δ −18.07 (s, 1P). High resolution EI-MS calcd for $C_{26}H_{34}N_4O_5P^+$: 513.22744. Found: 513.22668.

*Synthesis of 4-[[4-[Bis(2-hydroxyethyl)amino]phenyl]diazenyl]-1-[4-(diethoxyphosphoryl) benzyl]pyridinium Bromide (**5**).* To a solution of 4-[[4-[bis(2-hydroxyethyl)amino]phenyl]diazenyl]-1-(4-phosphonobenzyl) pyridinium bromide (**4**) (0.297 g, 0.5 mmol) in anhydrous CH_2Cl_2 (30 mL) was added trimethylbromosilane (10 equiv, 0.66 mL) dropwise over 10 min. The mixture was then stirred overnight at room temperature under a nitrogen atmosphere. After completion of the reaction, the solvent was evaporated and the residue was dissolved in methanol (5 mL). Filtration and evaporation of the solvent afforded 0.29 g of the pure final product **PAE** as a red powder. ^{1}H NMR (500 MHz, DMSO-d_6): δ 9.05 (d, 2H, J_{H-H} = 7 Hz), 8.12 (d, 2H, J_{H-H} = 6.5 Hz), 7.90 (d, 2H, J_{H-H} = 9.5 Hz), 7.70−7.74 (m, 2H), 7.55−7.57 (m, 2H), 7.10 (d, 2H, J_{H-H} = 9.5 Hz), 5.04 (s, 2H), 3.65−3.74 (m, 8H). ^{31}P NMR (400 MHz, DMSO-d_6): δ −12.83 (s, 1P). High resolution EI-MS calcd for $C_{22}H_{26}N_4O_5P^+$: 457.16408. Found: 457.16532.

Fabrication and Characterization of Zirconia-Phosphonate Self-Assembled Nanodielectric (Zr-SAND) Films. *Zr-SAND Film Fabrication.* Heavily n-doped silicon (Montco Silicon Tech, Inc.) substrates were cleaned in EtOH (Aldrich, absolute, 200 proof) by sonication for 2 min and then dried under flowing nitrogen, followed by oxygen plasma treatment for 5 min to remove organic contamination and to improve the wettability. A 0.01 M absolute ethanol solution of zirconium(IV) chloride was prepared, followed by the addition of a mixture of nitric acid and DI water (molar ratio; $ZrCl_4$:HNO_3:H_2O = 1:10:10). The resulting zirconium precursor solution was then heated to 50 °C for 3 h to accelerate hydrolysis. For the ultrathin ZrO_2 primer film fabrication, the hydroxyl-functionalized Si/SiO_2 substrates were spin-coated with the zirconium precursor solution at 5000 rpm for 30 s, and then cured at 150 °C for 20 min. This procedure was repeated twice to complete the ZrO_2 primer layer. For deposition of the first phosphonic-acid based π-electron (**PAE**) layer, the substrate with the primer layer was immersed in a solution of the phosphonic-acid based π-electron precursor (**PAE**; 3.0 mM in methanol) at 60 °C for 30 min. After rinsing with MeOH, the samples were the dried under a nitrogen stream. The third step of the growth process was accomplished by again spin-coating the zirconium precursor, followed by curing at 150 °C for 20 min to form a ZrO_2 interlayer. Repeating the second and third steps results in thicker multilayer formation. All zirconium precursor solutions were filtered through a 0.2 μm pore size PTFE membrane syringe filter prior to spin-coating and were spin-coated under a controlled atmosphere of less than 10% relative humidity (measured with a Fisher Scientific Traceable Hygrometer-Thermometer-Dew Point probe). For MIS structures, gold electrodes were directly deposited (200 μm × 200 μm) onto each Zr-SAND specimen through a shadow mask.

Zr-SAND Film Microstructure Characterization. Optical absorption spectra of Zr-SAND films deposited on glass were acquired with a Varian Cary 5E spectrophotometer. The film thicknesses of Zr-SAND films on Si wafers were analyzed by X-ray reflectivity (XRR) using wavelength λ = 0.1541 nm Cu Kα radiation on an 18 kW Rigaku ATX-G diffractometer at Northwestern University's X-ray Diffraction Facility. The structural details of the electron density profile are obtained by fitting the XRR data to a multilayer model calculated by the Abeles matrix method using the Motofit software package.[53,54] Each bilayer, n, is defined by its thickness, d_n, electron density, ρ_n, and interface roughness, σ_n, to generate a complete

Scheme 2. Fabrication Procedure for Zr-Phosphonate Self-Assembled Nanodielectric (Zr-SAND) Multilayers

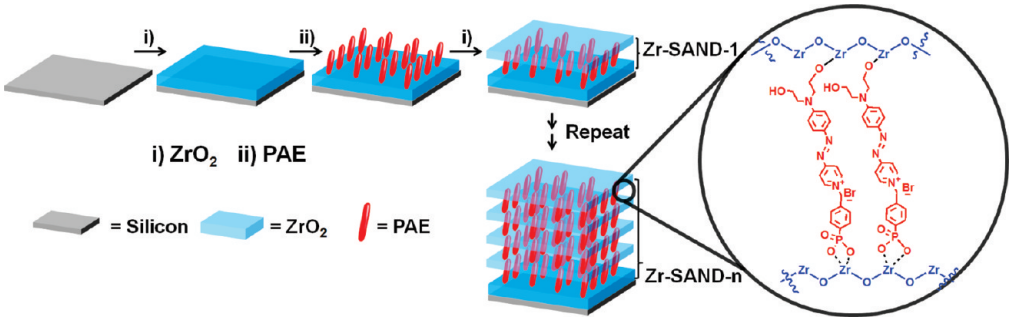

electron density profile $\rho(z)$. The zirconia-phosphonate self-assembled nanodielectrics are referred to in the rest of this Article as **Zr-SANDs**. Four kinds of multilayer systems were prepared and analyzed: Zr-SAND-*n*, where *n* is the number of bilayers and *n* = 1, 2, 3, and 4. Zr-SAND-1 was modeled as 3 slabs (primer ZrO_2 layer, **PAE** layer, and ZrO_2 interlayer) with a Si substrate and an air superstrate. For thicker multilayers, two slabs were added to model each additional layer, corresponding to the organic and inorganic components. Interparameter constraints and batch-fitting procedures were employed to reduce the number of free parameters, limit solutions to a physically reasonable range, and enforce structural consistency between multilayer models. Cross-sectional TEM samples were prepared and imaged using a JEOL-2100F scanning/transmission electron microscope (S/TEM) and a Hitachi HD-2300A scanning electron microscope (STEM), with both bright-field (BF) and high-angle annular dark-field (HAADF) detectors. The morphologies of all thin films were evaluated by atomic force microscopy (AFM) using a JEOL-5200 scanning probe microscope with silicon cantilevers operating in the tapping mode.

Fabrication of Thin-Film Transistors Using Organic/Inorganic Semiconductors on Zr-SAND Films. *Pentacene (p-type Organic Semiconductor) Thin-Film Transistor Fabrication.* Bottom gate/top contact OTFTs were fabricated by vacuum deposition of pentacene (50 nm, 5 × 10^{-6} Torr 0.05 nm/s) onto Zr-SANDs having four different thicknesses (Zr-SAND-1, 2, 3, and 4). To complete the TFT structure, gold S/D electrodes were vacuum-deposited (50 nm, 0.02 nm/s) through a shadow mask (L = 100 μm, W = 2000 μm).

Zinc Tin Oxide (n-type Inorganic Semiconductor) Thin-Film Transistor Fabrication. For inorganic TFTs, the precursor solution was prepared as follows. Zinc acetate dihydrate (0.3 M) and tin chloride(II) (0.3 M) in a 4:6 molar ratio were dissolved in 1 mL of 2-methoxyethanol (99%, Aldrich) in a 2.5 mL vial. To this solution, ethanolamine (0.3 mmol) as a stabilizer was added to the vial, and the resulting clear solutions were stirred for 30 min at room temperature before spin-coating. The zinc tin oxide precursor solution was then spin-coated (3000 rpm, 30 s) onto the Zr-SAND substrates. Subsequently, the spin-coated films were annealed on the hot plate at the desired temperature (400 °C) for 5 min. To complete the TFT structure, aluminum S/D electrodes were vacuum-deposited (30 nm, 1 nm/s) through a shadow mask (L = 100 μm, W = 2000 μm).

Fabrication of Organic Thin-Film Transistors on Phosphonic Acid Self-Assembled Monolayer (PA-SAMs)-Treated Zr-SAND Film. *Phosphonic Acid Self-Assembled Monolayer (PA-SAM) Preparation on Zr-SAND.* The Zr-SAND-3 film was prepared by the procedures described above. Four phosphonic acids having different alkyl chain lengths were selected and were as follows: *n*-hexyl (PA-C6), *n*-dodecyl (PA-C12), *n*-tetradecyl (PA-C14), and *n*-octadecyl (PA-C18) phosphonic acid (Figure 12). Phosphonic acid self-assembled monolayers (PA-SAMs) were prepared by immersing the substrates into solutions of 2.0 mM of PA-C6, PA-C12, PA-C14, and PA-C18 (Alfa Aesar) in absolute EtOH. The substrates were kept in the phosphonic acid solutions overnight, followed by rinsing with EtOH, and drying under a nitrogen stream.

Organic Thin-Film Transistor Fabrication (p- and n-type) and Characterization on PA-SAM-treated Zr-SAND Films. After depositing various PA-SAMs (PA-C6, PA-C12, PA-C14, and PA-C18) on Zr-SAND-3, advancing aqueous contact angles were measured with DI. For OTFT structures, bottom gate/top contact OTFTs were fabricated by vacuum deposition of pentacene (50 nm, 5 × 10^{-6} Torr 0.05 nm/s) as a p-type and **PDIF-CN$_2$** (50 nm, 5 × 10^{-6} Torr 0.03 nm/s) as an n-type semiconductor onto each PA-SAMs treated Zr-SAND-3. To complete the OTFT structure, gold S/D electrodes were vacuum-deposited (50 nm, 0.02 nm/s) through a shadow mask (L = 100 μm, W = 2000 μm). The morphologies of the various pentacene films were evaluated by atomic force microscopy (AFM) using a JEOL-5200 scanning probe microscope with silicon cantilevers operating in the tapping mode. X-ray diffraction (XRD) patterns of pentacene thin-film (50 nm) were measured on a Rigaku ATX-G Thin-Film Diffraction Workstation using Cu Kα radiation.

TFT Measurements and Characterization of Dielectrics and Thin-Film Transistors. MIS direct current measurements and OTFT measurements were carried out under ambient conditions using a Signatone probestation interfaced to a Keithley 6430 Sub-Femtoamp Remote Source Meter and a Keithley 2400 source meter with a locally written LabVIEW program. An impedance analyzer (HP 4192A) was used for capacitance measurements.

RESULTS AND DISCUSSION

Here, we present a detailed investigation of the properties of zirconia-phosphonate self-assembled nanodielectrics (Zr-SANDs) specifically designed to form multilayer structures incorporating highly polarizable phosphonic acid-based π-electron (PAE) layers interleaved with ultrathin high-k zirconium oxide (ZrO_2) layers. To verify that structurally well-defined building blocks can be manipulated for multilayer fabrication, Zr-SANDs are first examined by a full complement of microstructural characterization techniques. Following this, experimental dielectric properties such as electrical insulating and capacitance properties as well as thermal stability during high temperature (400 °C) anneal processing are also presented. Next, the TFT response with representative organic and inorganic semiconductors is examined. Finally, correlations between the OTFT response and the structures of self-assembled monolayers (SAMs) deposited directly on the Zr-SAND surface are examined, and comparisons made. Importantly, it will be seen that this deposition technique results in smooth, robust films at low processing temperatures (~150 °C), and the films exhibit excellent electrical insulating and dielectric properties. These Zr-SANDs are compatible with n-, p-type and organic, inorganic semiconductors and enable significantly reduced TFT operating voltages as compared to conventional SiO_2 dielectrics.

Fabrication and Characterization of Zirconia-Phosphonate Self-Assembled Nanodielectric (Zr-SAND) Films. The phosphonic

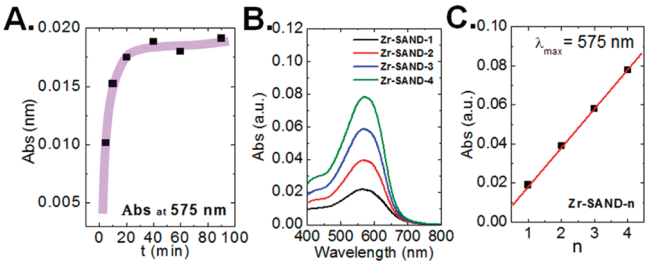

Figure 2. (A) Optical spectroscopic data as a function of reaction/deposition time for optimizing the formation of a chromophore monolayer. (B) UV−vis absorption spectra of Zr-SAND-1 (black), Zr-SAND-2 (red), Zr-SAND-3 (blue), and Zr-SAND-4 (green) samples. (C) Optical absorption spectra of Zr-SAND-n at 575 nm as a function of the number of bilayers (Zr-SAND-1, 2, 3, and 4).

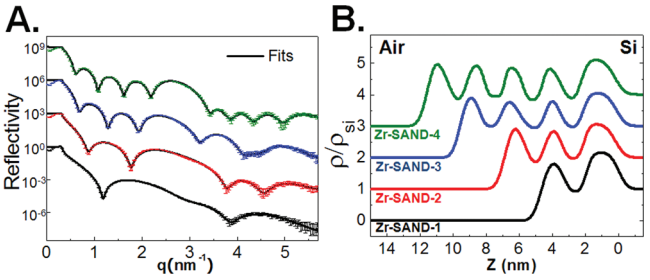

Figure 3. (A) X-ray reflectivity data and theoretical fit as a function of q for Zr-SAND-n multilayer films with number of bilayers n = 1 (black), n = 2 (red), n = 3 (blue), and n = 4 (green). (B) The electron density profiles (normalized to ρ_{Si}), corresponding to the fits in (A) as a function of height z above the Si substrate surface.

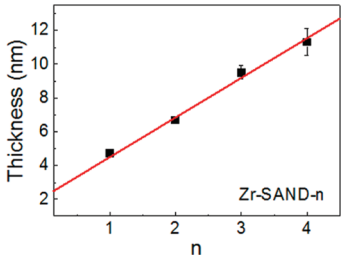

Figure 4. Specular X-ray reflectivity (XRR)-derived film thickness (nm) data as a function of the number of bilayers, n, in the multilayer films Zr-SAND-1−4 as prepared via the procedure of Scheme 2. The solid line is the fit by linear regression, indicating an average bilayer thickness of 2.4 nm.

acid-based π-electron building block (**PAE**) 4-((4-(bis(2-hydroxyethyl)amino)phenyl)diazenyl)-1-(4-(diethoxyphosphoryl)benzyl) pyridinium bromide (**5**; Scheme 1) was synthesized as described in the Experimental Section and was characterized by conventional analytical techniques (^{1}H NMR, ^{13}C NMR, ^{31}P NMR, and HR-MS). The zirconia-phosphonate self-assembled nanodielectrics (Zr-SANDs) were fabricated according to Scheme 2, consisting of depositing the ZrO_2 primer layer on a silicon wafer, followed by iterative deposition of the phosphonic acid-based π-electron (**PAE**) layer and the ZrO_2 interlayer for capping and multifunction. The ultrathin high-k ZrO_2 primer layer and interlayer bonding enhance the orientational stability of the PAE molecules and minimize capacitance degradation of the parallel multilayer structure while enhancing leakage characteristics. Thus, pretreated heavily n-doped silicon was spin-coated using the zirconium precursor solution described above, and then cured at 150 °C for 20 min to complete the primer layer. For Zr-SAND-1 fabrication, the primer ZrO_2 layer-coated substrate was immersed in a 3 mM methanol solution of the phosphonic acid-based π-electron (**PAE**) molecule at 60 °C for 30 min, rinsed with methanol, and the ZrO_2 interlayer was then deposited by the same method used for the primer layer. Zr-SAND-2, 3, and 4 structures were formed by alternating repetition of the **PAE** and ultrathin ZrO_2 bilayer depositions. **PAE** solutions can be reused multiple times without any noticeable detrimental effects on film quality.

The present iterative two-step process (**PAE** + ZrO_2 layer) (Scheme 2) and the resulting multilayer structural regularity were characterized by a full complement of physicochemical techniques: (1) transmission optical spectroscopy (UV−vis) to characterize assembly chemistry and microstructural regularity, (2) X-ray reflectivity (XRR) to characterize film thickness, density, and interfacial roughness, (3) transmission electron microscopy (TEM) to characterize film thickness and microstructural regularity, and (4) atomic force microscopy (AFM) to characterize surface morphology and roughness.

The **PAE** deposition kinetics from MeOH solution onto substrates were monitored by UV−vis spectroscopy to optimize reaction conditions. Figure 2A shows the deposition kinetics at 60 °C. The **PAE** optical transition at 575 nm reaches a maximum after 30 min at 60 °C, and longer reaction times result in a constant absorption, meaning that a densely packed molecular assembly of **PAE** is achieved. No other bands or shifts in the optical absorbance maxima are observed, arguing against significant chromophore aggregation or decomposition (Figure 2B). Furthermore, the UV−vis measurements unambiguously demonstrate a linear dependence of the HOMO−LUMO CT chromophore optical absorbance at 575 nm on Zr-SAND-1−4, demonstrating that essentially equal quantities of uniformly aligned chromophore units are incorporated in each sublayer up to Zr-SAND-4 bilayers.

The XRR data and analysis are shown in Figure 3A as a function of the out-of-plane scattering vector $q = 4\pi \sin\theta/\lambda$, with least-squares best-fit models calculated with Abeles matrix method using the Motofit software package (Nelson).[53,54] The data exhibit the classical Kiessig fringes expected from similar organic−inorganic hybrid multilayers with alternating low- and high-electron density layers.[55] The corresponding fits for each data set are shown overlaid on the data. Easily observable is the emergence of the first-order multilayer Bragg peak at q = ~2.65 nm^{-1} (d = ~2.35 nm) as the number of layers increases. In Figure 3B, the extracted electron density profiles, normalized to ρ_{Si}, reveal highly ordered multilayers, which are consistent from sample to sample in terms of electron density, roughness, and thickness. Well-defined ZrO_2/**PAE** layer progressions are evident from the strong oscillations in the electron density profile. Additionally, all of the ZrO_2 and **PAE** interfaces are at comparable positions in z from sample to sample, indicating highly controlled, sequential deposition. The total thicknesses of the Zr-SAND-1, 2, 3, and 4 films are found to be 4.7 ± 0.1, 6.7 ± 0.1, 9.5 ± 0.2, and 11.3 ± 0.8 nm, respectively, as derived from the individual electron density profiles themselves,[56] and increase linearly with increasing numbers of bilayers, n (Figure 4). A linear fit of the thickness as a function of n linear regression reveals an average bilayer (PAE + ZrO_2 interlayer) thickness of 2.4 ± 0.1 nm, with d_{PAE}:d_{ZrO2} ~1.6:1 and the ZrO_2 primer layer thickness of 2.1 ± 0.2 nm. The electron density minima in the electron

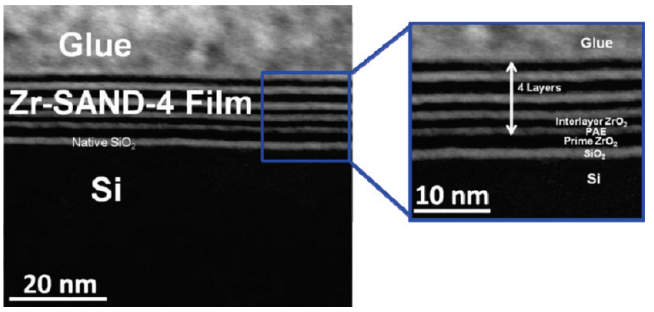

Figure 5. Cross-section TEM image of the Si/Zr-SAND-4 film interface. Labels indicate the layer identities.

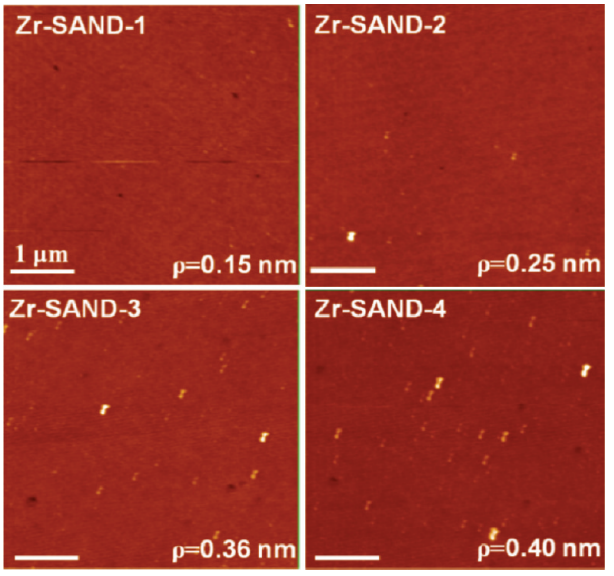

Figure 6. AFM images at 5 × 5 μm scan area of Zr-SAND-1−4 films. The space bar indicates 1 μm, and ρ is rms roughness.

density profiles correspond to the organic **PAE** layer and are found to be approximately that of bulk Si; however, this value is artificially high because the interface roughnesses are on the order of the **PAE** layer thickness. The ZrO_2 layers have electron densities that are nearly twice that of bulk Si, but again it is possible to see the effects of the interface roughness in the reduced electron densities of the thinner ZrO_2 layers deposited on the **PAE** as compared to that of the ZrO_2 base layer. Finally, interfaces were found to have rms roughnesses of less than 0.5 nm from the data fitting. A cross-sectional high-angle annular dark-field scanning transmission electron microscopy (HAADF STEM) image of Zr-SAND-4 (Figure 5) reveals a continuous and uniform contrast for the individual phases, which provides direct observation of the superlattice structures and confirms the expectations for the individual **PAE** and ZrO_2 layers in the multilayer film structure. The primer ZrO_2 is ~2 nm thick on top of native Si oxide layer (as expected by the double coating), and the **PAE** layer thickness is 1.5 ± 0.1 nm, in agreement with the computed molecular lengths and previous results.[48,57] The subsequent top ZrO_2 layer is ~1 nm thick. The thicknesses of the Zr-SANDs can be controlled by adjusting the number of **PAE** and ultrathin ZrO_2 bilayers. Note that the measured thickness of ~12 nm for Zr-SAND-4 from the TEM images is in good

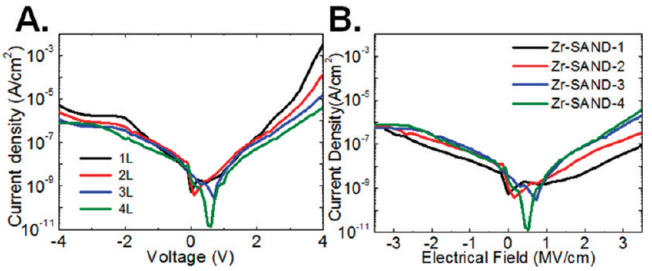

Figure 7. (A) Leakage current density versus voltage (J vs V) and (B) leakage current density versus electric field (J vs E) for Zr-SAND-1−4.

agreement with the aforementioned XRR results. Atomic force microscopy (AFM) images (Figure 6) of the Zr-SAND-1−4 films demonstrate continuous, crack/pinhole-free surface morphologies (maximum root-mean-square (rms) roughness of ~0.5 nm).

To assess the dielectric properties of the Zr-SANDs, metal−insulator−semiconductor (MIS) sandwich structure devices were fabricated by thermal Au electrode deposition (dimension: 200 μm × 200 μm) on the Zr-SANDs-coated n^{++}-Si substrates. Figure 7 shows typical current density versus voltage ($J-V$) and current density versus electric field ($J-E$) plots for MIS structures fabricated with four different thicknesses (Zr-SAND-1, 2, 3, and 4). The leakage current density of these films progressively decreases for the same applied voltage (±4 V) as the number of layers is increased due to the increased thickness. Note, however, that the leakage current density for the same electric field increases with the number of layers, then saturates at ~10^{-7} A/cm^2 at 2 MV/cm beyond Zr-SAND-3. The lower leakage current density for Zr-SAND-1 or -2 versus the thicker films appears to arise from synergistic effects involving additional leakage barriers such as those provided by the native oxide and the ZrO_2 primer layer. However, note that this effect is reduced with increasing layer numbers because the contribution of the additional leakage barrier becomes negligible as the dielectric thickness is increased. Furthermore, the leakage current densities of the combined **PAE**+ZrO_2 hybrid films are at least 10× lower (<1×10^{-6} A/cm^2, 2 MV/cm) than that of bulk ZrO_2 films (~1×10^{-5} A/cm^2, 2 MV/cm) prepared by sol−gel methods at the same processing temperature (150 °C).[58] All of these data are summarized in Table 1.

Capacitance−frequency ($C-f$) measurements were performed on the MIS structures, and the measured capacitances are 750 (Zr-SAND-1), 633 (Zr-SAND-2), 535 (Zr-SAND-3), and 465 nF/cm^2 (Zr-SAND-4) at 10 kHz (Figure 8). As the number of layers is increased, the capacitance values decrease due to the increased thickness. The multilayer dielectric in the n^{+2}-Si/Zr-SAND [primer ZrO_2/(PAE/interlayer ZrO_2)$_n$, n (the number of bilayer) = 1, 2, 3, and 4]/Au MIS devices can be modeled as capacitors in series, according to eq 3.

$$\left(\frac{1}{C_i}\right) = \left(\frac{1}{C_{SiO_2}} + \frac{1}{C_{p\text{-}ZrO_2}}\right) + n\cdot\left(\frac{1}{C_{PAE}} + \frac{1}{C_{i\text{-}ZrO_2}}\right) \quad (3)$$

where n is the number of bilayers, SiO_2 is the native oxide on the Si wafer, p-ZrO_2 is the ZrO_2 primer layer, i-ZrO_2 is the ZrO_2 interlayer, and PAE is the phosphonic-acid-based π-electron layer. The capacitances of the native oxide and ZrO_2 primer layer on the Si bottom electrode are 1380 and 4425 nF/cm^2, respectively, assuming a 2.5 nm thick SiO_2 (k = 3.9) and 2 nm

Table 1. Summary of Film and Dielectric Properties for Zr-SAND-1−4 Films

	thickness (nm)	roughness (nm)	J (A/cm^2) at 2 MV/cm	C_i (nF/cm^2)
Zr-SAND-1	4.7 ± 0.1	0.15	7×10^{-8}	750
Zr-SAND-2	6.7 ± 0.1	0.25	2×10^{-7}	633
Zr-SAND-3	9.5 ± 0.2	0.36	3×10^{-7}	535
Zr-SAND-4	11.3 ± 0.8	0.40	3×10^{-7}	465

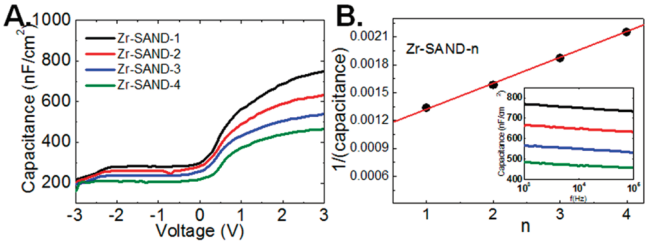

Figure 8. (A) Capacitance versus voltage plots measured at 10 kHz, and (B) inverse capacitance versus number of Zr-SAND bilayers. Inset: Capacitance versus frequency plots measured at 3.0 V for Zr-SAND-1−4.

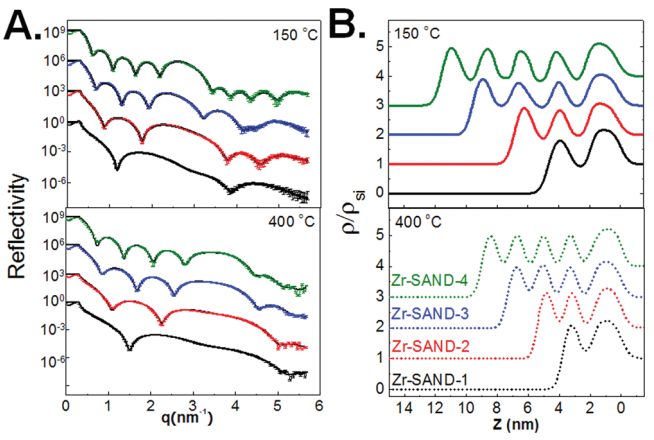

Figure 9. (A) X-ray reflectivity data and theoretical fits for control and thermally annealed Zr-SANDmultilayers as a function of q. (B) The electron density profiles (normalized to ρ_{Si}), corresponding to the fits in (A) as a function of height z above the Si substrate surface.

thick ZrO_2 layer ($k = 10$),[58] respectively. From the accumulation regime capacitances, the C_i of each Zr-SAND is measured as 465−750 nF/cm^2 at 10 kHz, yielding a PAE dielectric constant of ∼7 for the entire multilayer structure. The reciprocal value of C_i versus Zr-SAND-n (n = 1, 2, 3, and 4) plot shows a linear increase with the number of bilayers, which supports a regularly defined multilayer structure.

Thermal Stability of the Zr-SAND under High Annealing Temperature Conditions. Prior to Zr-SAND-based inorganic TFT fabrication, the thermal stability of the Zr-SAND dielectrics under ZTO annealing conditions was investigated in MIS capacitor structures. The n$^+$-Si/Zr-SAND substrates were thermally annealed at 400 °C, which is the same temperature as ZTO thin films for 5 min in air, and Au dot contacts then thermally evaporated through a shadow mask (200 × 200 mm^2). Next, the leakage current density (J_{leak}) versus voltage (or electric field) and capacitance versus voltage (or frequency) of the control Zr-SAND-4 and thermally annealed Zr-SAND-4 were measured in

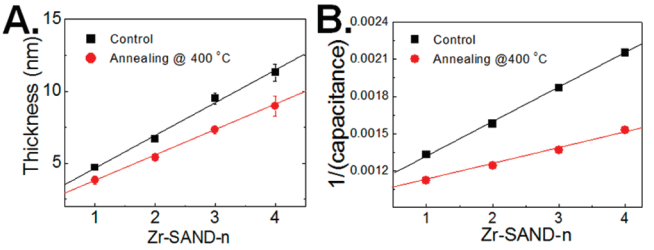

Figure 10. (A) X-ray reflectivity (XRR)-derived film thickness and (B) inverse capacitance versus number of Zr-SAND bilayers for the control and thermal annealed Zr-SAND multilayer samples.

the same bias window (−4 to +4 V). As compared to the control Zr-SAND-4 film (∼6 × 10^{-6} A/cm^2 at 4 V), the leakage current density increases slightly at the same applied voltage, after annealing at 400 °C in air (∼3 × 10^{-5} A/cm^2 at 4 V, Figure S1A). The capacitance of the Zr-SAND-4 film likewise increases as the annealing temperature is increased, from 465 (control) to 650 nF/cm^2 (400 °C; Figure S2). To further understand leakage current and capacitance variation during annealing, the microstructure of Zr-SAND-4 before annealing at high temperature and after thermally annealing at 400 °C was investigated by X-ray reflectivity (XRR). The XRR data and the extracted electron density profiles for control Zr-SANDs and high-temperature annealed Zr-SANDs are shown in Figure 9, with the best fits. The analysis of the XRR data reveals that the highly ordered multilayer structure persists after thermal annealing at 400 °C. However, as compared to the control Zr-SAND films, the thicknesses are reduced upon thermal annealing by as much as 20% versus the control Zr-SAND film (Figure 10A). This contraction is similar to that in silane-based conventional SAND dielectric films.[59] Note that while the film becomes thinner and denser after thermal annealing, the microstructural data and reciprocal C_i^{-1} versus Zr-SAND-n (n = 1, 2, 3, and 4) plot (Figure 10B) demonstrates that well-defined superlattice structures are preserved in the high temperature annealing. Therefore, the increased capacitance is reasonably associated with the decreased Zr-SAND film thickness. Note that the leakage current density increases slightly after 400 °C annealing for the same bias window and may simply reflect the film thickness reduction. Figure S1B plots the leakage current density versus electric field, demonstrating the similar behavior of the leakage current density at the same electric field between control and thermal annealed Zr-SAND-4 film. These results provide clear evidence that nanoscopic SAND films exhibit remarkable thermal and dielectric stability under ambient, rendering them suitable for high-temperature film growth/annealing processes.

Fabrication and Characterization of Thin-Film Transistors Using Organic or Inorganic Semiconductors on Zirconia-Phosphonate Self-Assembled Nanodielectric (Zr-SAND) Films. Given the excellent dielectric properties of Zr-SANDs, TFTs were next fabricated with representative organic (pentacene; **P5**) and inorganic (zinc tin oxide; **ZTO**) semiconductors on

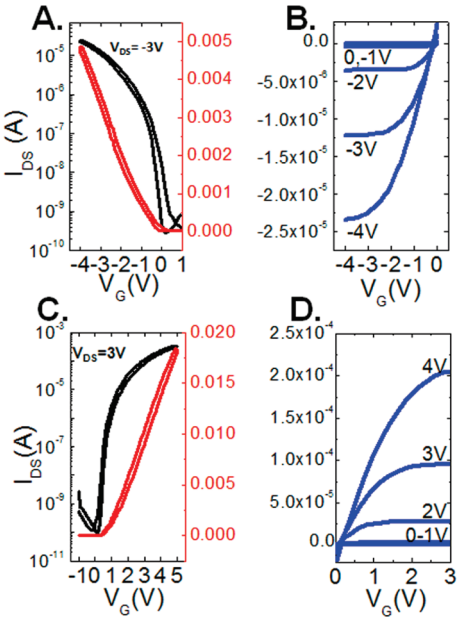

Figure 11. (A) Transfer plots and (B) output plots for pentacene OTFTs. (C) Transfer plots and (D) output plots for ZTO TFTs based on Zr-SAND-4.

Table 2. Carrier Mobility (μ, $cm^2\ V^{-1}\ s^{-1}$), Threshold Voltage (V_t), and Current On/Off Ratio (I_{on}/I_{off}) Data for TFT Devices Fabricated Using Pentacene and Zinc Tin Oxide as the p-type Organic and n-type Inorganic Semiconductors on Zr-SAND-1−4 Films

	P5			ZTO		
	μ ($cm^2\ V^{-1}\ s^{-1}$)	V_t	I_{on}/I_{off}	μ ($cm^2\ V^{-1}\ s^{-1}$)	V_t	I_{on}/I_{off}
Zr-SAND-1	0.32 ± 0.02	−0.5	10^4	3.0 ± 0.1	0.9	10^5
Zr-SAND-2	0.35 ± 0.02	−0.7	10^5	3.3 ± 0.1	1.0	10^6
Zr-SAND-3	0.36 ± 0.01	−0.8	10^5	3.4 ± 0.1	1.1	10^7
Zr-SAND-4	0.38 ± 0.01	−0.9	10^5	3.5 ± 0.1	1.1	10^7

Zr-SANDs by vacuum vapor deposition and spin-coating, respectively. All devices exhibit reproducible $I-V$ characteristics at low bias (<±4 V). Typical $I-V$ plots for TFTs on Zr-SAND-4 are shown in Figure 11, and Table 2 summarizes performance parameters as a function of semiconductor on Zr-SAND dielectrics having various thicknesses. Using the above capacitances and device geometry (L = 100 μm, and W = 2000 μm), these **P5** OTFTs devices exhibit good performance with hole mobilities of 0.35−0.38 $cm^2\ V^{-1}\ s^{-1}$, low threshold voltages (−0.5 to −0.9 V), and on−off current ratios of 10^4-10^5 on Zr-SAND-1−4. The **ZTO** TFTs fabricated with Zr-SAND exhibit excellent $I-V$ characteristics with classical/crisp linear pinch-off curves and saturation at very low operating voltages (<4.0 V). Analysis of the **ZTO**-TFT electrical response reveals large saturation-regime field-effect mobilities of 3.0−3.5 $cm^2\ V^{-1}\ s^{-1}$, and excellent on−off current ratios of 10^5-10^7. These carrier mobilities are comparable to or greater than those of control devices fabricated with a conventional 300 nm thick SiO_2 gate dielectric (mobility ~0.26 and 1.8 $cm^2\ V^{-1}\ s^{-1}$ for **P5** and **ZTO**, respectively), and their operating voltages (<±4 V) are much lower than on SiO_2 (±100 V),[60−63] reflecting the greater capacitance of the Zr-SANDs versus a conventional SiO_2 gate dielectric.

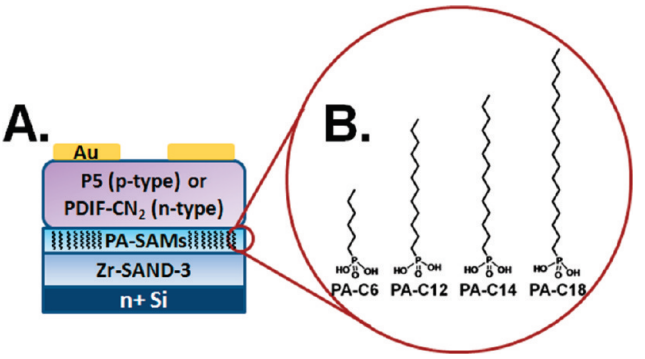

Figure 12. (A) Schematic view of a top contact OTFT using different *n*-alkyl PA-SAM/Zr-SAND gate dielectrics. (B) Chemical structures of the *n*-alkyl PA-SAMs used in this study: *n*-hexylphosphonic acid (PA-C6), *n*-dodecylphosphonic acid (PA-C12), *n*-tetradecylphosphonic acid (PA-C14), *n*-octadecylphosphonic acid (PA-C18).

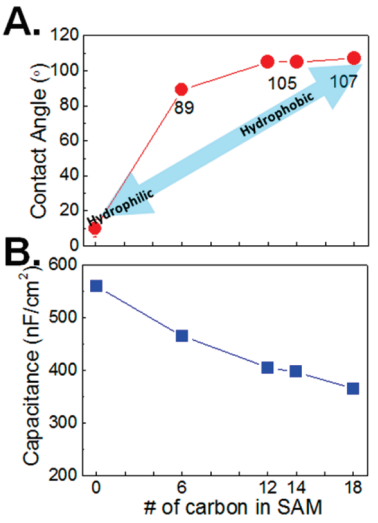

Figure 13. Variation in (A) aqueous contact angle (deg) and (B) capacitance as a function of the number of carbon atoms in the *n*-alkyl phosphonic acid SAMs deposited on Zr-SAND-3 films.

Fabrication and Characterization of Organic Thin-Film Transistors on Phosphonic-Acid Self-Assembled Monolayer (PA-SAM)-Functionalized Zr-SANDs. The present zirconia-phosphonate self-assembled nanodielectrics (Zr-SANDs) have a ZrO_2 surface which is decidedly hydrophilic (advancing aqueous contact angle <10°). Note that this characteristic of these high-*k* inorganic materials negatively affects organic semiconductor (OSC)-based TFT device performance through a combination of charge carrier surface trap sites associated with −OH groups, induced ionic polarization between charge carriers, and the high-*k* ionic lattice.[64−66] To address these limitations, such high-*k* oxide surfaces are typically planarized with a polymer dielectric leaving a nonpolar low-*k* surface, which is generally more compatible with standard OSCs;[67−69] however, the addition of a thicker polymer film reduces the capacitance. Another promising approach is to deposit nanoscopic self-assembled monolayers (SAMs), which are molecular films that spontaneously form by the adsorption of an organic surfactant on a solid substrate from the gas or solution

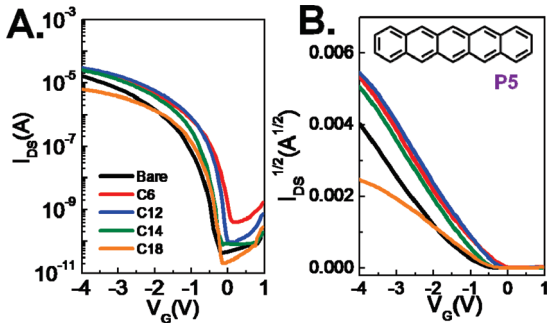

Figure 14. (A) Transfer characteristics and (B) $I_{DS}^{1/2}-V_G$ plots of **P5** TFTs fabricated on Zr-SAND-3 capped with the indicated PA-SAMs. The gate voltage is swept at a constant drain−source voltage $V_{DS} = -3$ V. Inset: Chemical structure of pentacene (**P5**).

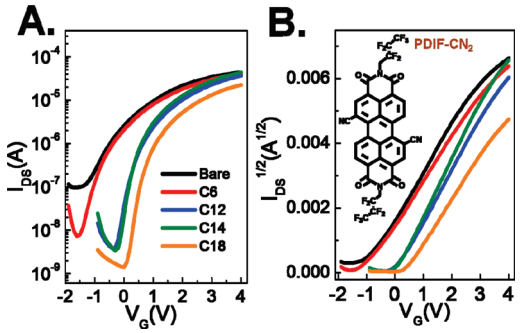

Figure 15. (A) Transfer characteristics and (B) $I_{DS}^{1/2}-V_G$ plots of **PDIF-CN$_2$** TFTs fabricated on Zr-SAND-3 coated with the indicated PA-SAMs. The gate voltage is swept at a constant drain−source voltage $V_{DS} = 3$ V. Inset: Chemical structure of **PDIF-CN2**.

phase.[70,71] With the addition of a few nanometers thick SAM layer, the dielectric capacitance is not reduced as much as by a conventional polymer film. In addition, functional SAMs provide an effective method for controlling the dielectric surface properties that affect the growth of the overlying thin film crystal structure and morphology, and hence the OSC electrical properties and subsequent OTFT device performance.[28,32,72,73] Here we systematically investigate the relationship between the alkyl chain length of the phosphonic-acid SAMs (PA-SAMs) that coat the gate dielectric and the electrical performance characteristics of the resulting organic TFTs (Figure 12). Commercially available phosphonic acids with four different alkyl chain lengths, $CH_3(CH_2)_xPO(OH)_2$, x = 5, 11, 13, and 17, were selected and compared. The PA-SAMs were prepared by immersing substrates coated with Zr-SAND-3 in an absolute EtOH solution of the corresponding phosphonic acid at room temperature for 12 h. Next, the substrates were rinsed with EtOH and dried in a stream of nitrogen. The purified semiconductors pentacene (**P5**) and perylene diimide (**PDIF-CN$_2$**) were then vacuum-deposited to form 50 nm thick semiconductor layers on the PA-SAM-treated dielectric. Advancing aqueous contact-angle measurements using DI water show that due to *n*-alkyl PA-SAM formation, the ZrO_2 surface changes from hydrophilic (10°) to hydrophobic (89−107°) (Figure 13A). The slight decrease in aqueous contact angle from 105° for PA-C12 to 89° for PA-C6 may be a result of lower SAM densities on the substrate. SAMs derived from hydrocarbon chains having less than about 10 carbon atoms form

Table 3. Carrier Mobility (μ, cm^2 V^{-1} s^{-1}), Threshold Voltage (V_t), and Current On/Off Ratio (I_{on}/I_{off}) Data for TFT Devices Fabricated Using Pentacene and PDIF-CN$_2$ as Representative p- and n-type Organic Semiconductors on PA-SAMs/Zr-SAND-3

			P5			PDIF-CN$_2$		
	CA	C_i	μ	V_t	I_{on}/I_{off}	μ	V_t	I_{on}/I_{off}
Zr-SAND-3	<10	560	0.36	−1.0	10^5	0.36	−1.2	10^2
PA-C6	89	465	0.61	−0.7	10^5	0.41	−1.0	10^3
PA-C12	105	405	0.74	−0.6	10^6	0.63	0.02	10^4
PA-C14	105	398	0.68	−0.8	10^6	0.79	0.01	10^4
PA-C18	107	365	0.16	−0.5	10^5	0.64	0.3	10^4

mostly disordered films, possibly due to a lack of cohesive van der Waals interactions between the chains.[74,75] For SAM chains longer than about 10 carbon atoms, the cohesive forces are expected to be sufficiently strong to force the molecules into an almost upright position, yielding dense, well-ordered monolayers, and affording large aqueous contact angles (>105°).[74−77] Note, however, that the surface properties of all of the present PA-SAM functionalized Zr-SANDs are hydrophobic. The leakage current densities of the PA-SAM/Zr-SAND-3 films (Figure S3) are not significantly reduced at the same applied voltage (±4 V). However, the C_i of the PA-SAM/Zr-SAND-3 films (Figure 13B) decreases with increased SAM alkyl chain length from 560 nF/cm^2 for the bare Zr-SAND-3 film to 365 nF/cm^2 for PA-C18 due to the relatively low dielectric constant of the hydrocarbon chains.[28] AFM was used to characterize the morphology of the *n*-alkyl PA-SAMs assembled on Zr-SAND, revealing generally smooth films (rms roughness less than 0.5 nm) (Figure S4). Figures 14 and 15 show representative transfer plots for OTFTs fabricated with **P5** and **PDIF-CN$_2$** on PA-SAMs/Zr- SAND-3. These plots exhibit reproducible $I-V$ characteristics at low operating voltages (<±4.0 V) as well as excellent linear/saturation behavior. For the **P5** TFTs, Figure 14 shows that increasing the alkyl chain length from 6 to 14 carbon atoms causes the mobility to increase from 0.61 to 0.74 cm^2 V^{-1} s^{-1}, while further increasing the chain length to 18 carbon atoms causes the mobility to drop to 0.16 cm^2 V^{-1} s^{-1}. Note that the **P5** mobility on the bare Zr-SAND is only 0.36 cm^2 V^{-1} s^{-1} and therefore smaller than most of the OTFTs fabricated with PA-SAM functionalized Zr-SAND. All of these devices exhibit excellent on−off current ratios (up to 10^5). Figure 14B and Table 3 show that the threshold voltages (V_t) decrease from −1.0 V for **P5**-TFTs on bare Zr-SAND to −0.5 V for TFTs with PA-SAMs. The threshold voltage is closely related to the charge state at the organic semiconductor channel/gate dielectric interface as long as the entire semiconductor channel films contain about the same density of deep level defects.[66,78] Therefore, the threshold voltage depends strongly on the preparation of the surface on which the organic semiconductor is deposited. In general, SAM deposition before growing the organic semiconductor layers is likely to eliminate trap states on the dielectric surface.[72,73,78,79] Consequently, as compared to bare Zr-SAND substrate, the PA-SAM functionalized surfaces should provide lower trap state densities, resulting in lower threshold voltages and higher TFT mobilities.[80]

Using a similar dielectric modification process, we also investigated n-type organic transistors fabricated with **PDIF-CN$_2$** (Figure 15), also operating at low voltages (<4.0 V). The TFT electron mobilities increase as the PA alkyl chain length is

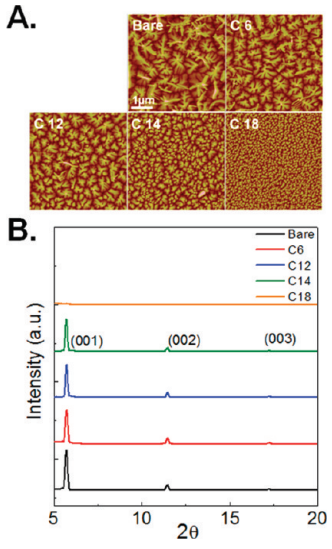

Figure 16. (A) AFM images and (B) $\theta-2\theta$ X-ray diffraction patterns of **P5** films grown on Zr-SAND-3 treated with the indicated PA-SAMs. AFM images are of areas 5 μm × 5 μm in size.

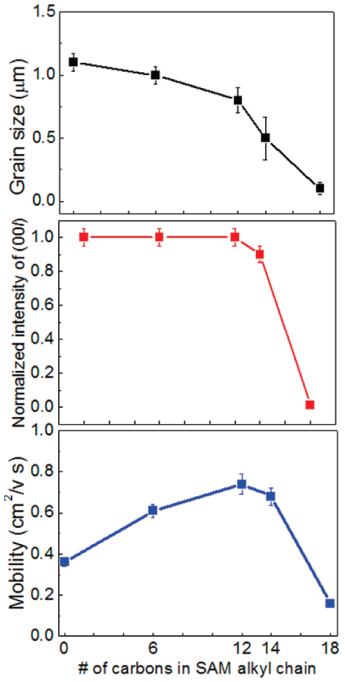

Figure 17. Variation in (A) pentacene film grain size, (B) normalized intensity of the pentacene film (00*l*) Bragg reflection, and (C) pentacene field-effect mobility in low-voltage OTFTs as a function of the number of alkyl carbon atoms in the *n*-alkyl phosphonic acid SAM on Zr-SAND-3.

increased from C6 to C14, but then fall slightly for the longest chain length (C18). Note that the TFT performance with the SAM-modified Zr-SAND is significantly greater than on a bare Zr-SAND surface. The on/off ratios are enhanced by ~100× with the PA-SAMs, and the threshold voltage shifts to positive (0.01 V) from negative (−1.2 V) as the PA-SAM chain length is increased. All of these data are summarized in Table 3.

Pentacene Morphology and OTFT Response Characteristics on PA-SAM-Functionalized Zr-SAND. Because OTFT charge transport is confined to the nanoscopic region at the semiconductor/dielectric interface, an optimized interface between the dielectric film and the semiconductor is clearly a prerequisite for optimum OTFT performance.[60,79] Especially for **P5**-based TFTs, their interfacial properties are closely related to the morphology and microstructure of the **P5** thin films, thereby strongly influencing their performance. We have found here that **P5** TFT characteristics depend significantly on the SAM alkyl chain lengths, and that PA-C12 or PA-C14 provide optimum performance for the **P5** semiconductor films in this study. We have evaluated the **P5** thin-film morphology by AFM and the **P5** thin-film crystallinity on the various PA-SAMs/Zr-SAND-3 by X-ray diffraction (XRD). Figure 16 compares the **P5** grain size and crystallinity of **P5** films grown on bare Zr-SAND-3, and on PA-C6, C12, C14, and C18/Zr-SAND-3. According to these data, the grain sizes of the **P5** thin films (approximately 1 μm) decrease slightly from bare Zr-SAND-3 to PA-C12, and then drop to ~0.5 μm on PA-C14-coated Zr-SAND-3. Eventually, the crystallite dimensions become very small (less than 0.1 μm) on the PA-C18/Zr-SAND-3. On PA-C14/Zr-SAND-3, the **P5** film has a grain size of approximately 0.5 ± 0.1 μm, which is significantly larger than in films on PA-C18/Zr-SAND-3. Figure 16B shows the XRD patterns of the **P5** films grown on PA-SAMs/Zr-SAND-3. The XRD data for **P5** films on PA-SAMs/Zr-SAND-3 feature a distinctive first-order reflection located at 2θ = 5.7°. Three characteristic features arising from the (00*l*) Bragg planes of the thin-film phase dominate the XRD patterns. These films on bare Zr-SAND-3 and on Zr-SAND-3 coated with PA-C6, PA-C12, and PA-C14 are highly crystalline because the first reflection is sharp and intense. In contrast, **P5** films grown on PA-C18 are far less crystalline. After functionalizing the Zr-SAND-3 with PA-SAMs, the device performance generally improves even though the grain size of the **P5** films is reduced somewhat as compared to the bare Zr-SAND-3 substrate. This performance enhancement when comparing PA-SAMs to bare Zr-SAND-3 (Table 3) verifies that the presence of the SAMs enhances the quality of the OSC/dielectric interface. The lower V_t and higher μ values observed for most *n*-alkyl PA-SAMs versus bare Zr-SAND-3 are consistent with the suppression of any adverse effects of the high-*k* dielectric surface on device performance by reduction of −OH trap sites on the surface.[66,78] When comparing TFT results between the different *n*-alkyl PA-SAMs, there are distinctive differences, particularly in mobility. Furthermore, there are systematic trends that are observed in μ when comparing PA-C12, PA-C14, and PA-C18/Zr-SAND-3 (Figure 17). As the number of carbon atoms of the SAM alkyl chain is increased from C12 to C18, the relative **P5** XRD diffraction intensities decrease and the grain sizes also decline, resulting in clear degradation of μ from 0.74 to 0.16 $cm^2 V^{-1} s^{-1}$. For the **P5** thin films on PA-C18, the grain size and XRD intensity fall significantly, resulting in very poor TFT performance. This trend is expected because it is known that, in general, small grain sizes and reduced film crystallinity depress μ due to drastically increased grain boundary densities.[81−84] Figure 17 shows the grain size, relative crystallinity, and mobility trends of the **P5** films grown on bare Zr-SAND-3, and on Zr-SAND-3 coated with PA-C6, PA-C12, PA-C14, and PA-C18.

Using the same SAM modification process, we also investigated n-type organic transistors using the semiconductor **PDIF-CN_2**. The OTFT performance with **PDIF-CN_2** shows behavior generally similar to that of the **P5** TFTs (Table 3). TFT mobilities with the SAM-modified Zr-SAND are substantially enhanced versus those on the bare Zr-SAND surface, and on/off ratios are enhanced by ~100× with the PA-SAMs. AFM and

XRD data (Figure S5) reveal similar **PDIF-CN$_2$** morphologies for SAM-coated Zr-SAND versus bare Zr-SAND. However, in terms of the threshold voltage, large shifts to positive (0.01 V) from negative (−1.2 V) voltages are observed as the PA-SAM chain length is increased. The systematic PA-SAM chain length increases result in substantially increased the electron carrier density in the transistor channel, inducing an abrupt shift in the threshold voltage toward more positive values. This relationship between the SAM-treated gate dielectric surface and the threshold voltage is similar to that observed in other p- and n-type organic TFTs with various SAM gate dielectrics.[80,85]

CONCLUSIONS

We have demonstrated here that a new solution-phase layer-by-layer growth method for self-assembled organic−inorganic multilayer dielectrics using phosphonic acid-based organic and zirconium-based inorganic precursors affords robust, smooth, adherent, insulating, pinhole-free, high-capacitance, thermally stable, ultrathin dielectric materials. These multilayer materials can be used for low operating voltage organic and inorganic semiconductor-based TFT devices as versatile gate dielectrics with excellent thermal stability. The advantages of the present growth method include accurate control of film thickness, large-area uniformity, highly conformal layering, and easily tunable interfacial properties. Furthermore, this method is an ideal fabrication technique for various organic−inorganic hybrid multilayer structures and should also be applicable to fabricating a variety of organic−inorganic hybrid superlattices, which facilitate novel materials processing for diverse applications.

ASSOCIATED CONTENT

Supporting Information. AFM images and dielectric performance data for selected dielectric materials. This material is available free of charge via the Internet at http://pubs.acs.org.

AUTHOR INFORMATION

Corresponding Author
a-facchetti@northwestern.edu; t-marks@northwestern.edu

ACKNOWLEDGMENT

This research was supported by the AFOSR (FA9550-08-1-0331) and the NSF MRSEC program (DMR-0520513) at Northwestern University. Microscopy studies were performed in the EPIC and NIFTI facilities of the NUANCE Center at Northwestern University. The NUANCE Center is supported by NSF-NSEC, NSF-MRSEC, the State of Illinois, and Northwestern University. This work made use of the J. B. Cohen X-ray Diffraction Facility supported by the MRSEC program of the National Science Foundation at the Materials Research Center at Northwestern University. We thank Dr. Jinsong Wu for the TEM image and helpful discussions.

REFERENCES

(1) Facchetti, A. *Chem. Mater.* **2011**, *23*, 733.
(2) Arias, A. C.; MacKenzie, J. D.; McCulloch, I.; Rivnay, J.; Salleo, A. *Chem. Rev.* **2010**, *110*, 3.
(3) Roberts, M. E.; Mannsfeld, S. C. B.; Queralto, N.; Reese, C.; Locklin, J.; Knoll, W.; Bao, Z. N. *Proc. Natl. Acad. Sci. U.S.A.* **2008**, *105*, 12134.
(4) Braga, D.; Horowitz, G. *Adv. Mater.* **2009**, *21*, 1473.
(5) Cho, J. H.; Lee, J.; Xia, Y.; Kim, B.; He, Y. Y.; Renn, M. J.; Lodge, T. P.; Frisbie, C. D. *Nat. Mater.* **2008**, *7*, 900.
(6) Klauk, H. *Organic Electronics: Materials, Manufacturing and Applications*; Wiley-VCH: Weinheim, 2006.
(7) Kagan, C. R.; Andry, P. *Thin-Film Transistors*; Marcel Dekker: New York, 2003.
(8) Sze, S. M.; Ng, K. K. *Physics of Semiconductor Devices*, 3rd ed.; Wiley-Interscience: Hoboken, NJ, 2007.
(9) Ramesh, R.; Schlom, D. G. *MRS Bull.* **2008**, *33*, 1006.
(10) Pal, B. N.; Dhar, B. M.; See, K. C.; Katz, H. E. *Nat. Mater.* **2009**, *8*, 898.
(11) Murphy, A. R.; Frechet, J. M. J. *Chem. Rev.* **2007**, *107*, 1066.
(12) Sekitani, T.; Zschieschang, U.; Klauk, H.; Someya, T. *Nat. Mater.* **2010**, *9*, 1015.
(13) Loo, Y. L.; McCulloch, I. *MRS Bull.* **2008**, *33*, 653.
(14) Marks, T. J. *MRS Bull.* **2010**, *35*, 1018.
(15) Facchetti, A. *Mater. Today* **2007**, *10*, 28.
(16) Yan, H.; Chen, Z. H.; Zheng, Y.; Newman, C.; Quinn, J. R.; Dotz, F.; Kastler, M.; Facchetti, A. *Nature* **2009**, *457*, 679.
(17) Zaumseil, J.; Sirringhaus, H. *Chem. Rev.* **2007**, *107*, 1296.
(18) Sun, Y. G.; Rogers, J. A. *Adv. Mater.* **2007**, *19*, 1897.
(19) Kim, F. S.; Guo, X. G.; Watson, M. D.; Jenekhe, S. A. *Adv. Mater.* **2010**, *22*, 478.
(20) Wong, W. W. H.; Singh, T. B.; Vak, D.; Pisula, W.; Yan, C.; Feng, X. L.; Williams, E. L.; Chan, K. L.; Mao, Q. H.; Jones, D. J.; Ma, C. Q.; Mullen, K.; Bauerle, P.; Holmes, A. B. *Adv. Funct. Mater.* **2010**, *20*, 927.
(21) Hutchison, G. R.; Ratner, M. A.; Marks, T. J. *J. Am. Chem. Soc.* **2005**, *127*, 2339.
(22) Letizia, J. A.; Salata, M. R.; Tribout, C. M.; Facchetti, A.; Ratner, M. A.; Marks, T. J. *J. Am. Chem. Soc.* **2008**, *130*, 9679.
(23) Facchetti, A.; Yoon, M. H.; Stern, C. L.; Katz, H. E.; Marks, T. J. *Angew. Chem., Int. Ed.* **2003**, *42*, 3900.
(24) Veres, J.; Ogier, S.; Lloyd, G.; de Leeuw, D. *Chem. Mater.* **2004**, *16*, 4543.
(25) Ortiz, R. P.; Facchetti, A.; Marks, T. J. *Chem. Rev.* **2010**, *110*, 205.
(26) Facchetti, A.; Yoon, M. H.; Marks, T. J. *Adv. Mater.* **2005**, *17*, 1705.
(27) Robertson, J. *Rep. Prog. Phys.* **2006**, *69*, 327.
(28) Acton, O.; Ting, G.; Ma, H.; Ka, J. W.; Yip, H. L.; Tucker, N. M.; Jen, A. K. Y. *Adv. Mater.* **2008**, *20*, 3697.
(29) Costescu, R. M.; Cahill, D. G.; Fabreguette, F. H.; Sechrist, Z. A.; George, S. M. *Science* **2004**, *303*, 989.
(30) Mitzi, D. B. *Chem. Mater.* **2001**, *13*, 3283.
(31) Klauk, H.; Zschieschang, U.; Pflaum, J.; Halik, M. *Nature* **2007**, *445*, 745.
(32) Zschieschang, U.; Ante, F.; Yamamoto, T.; Takimiya, K.; Kuwabara, H.; Ikeda, M.; Sekitani, T.; Someya, T.; Kern, K.; Klauk, H. *Adv. Mater.* **2010**, *22*, 982.
(33) Zschieschang, U.; Ante, F.; Schlorholz, M.; Schmidt, M.; Kern, K.; Klauk, H. *Adv. Mater.* **2010**, *22*, 4489.
(34) Acton, O.; Osaka, I.; Ting, G.; Hutchins, D.; Ma, H.; McCullough, R. D.; Jen, A. K. Y. *Appl. Phys. Lett.* **2009**, 95.
(35) Ting, G. G.; Acton, O.; Ma, H.; Ka, J. W.; Jen, A. K. Y. *Langmuir* **2009**, *25*, 2140.
(36) Park, Y. M.; Daniel, J.; Heeney, M.; Salleo, A. *Adv. Mater.* **2011**, *23*, 971.
(37) DiBenedetto, S. A.; Frattarelli, D.; Ratner, M. A.; Facchetti, A.; Marks, T. J. *J. Am. Chem. Soc.* **2008**, *130*, 7528.
(38) DiBenedetto, S. A.; Frattarelli, D. L.; Facchetti, A.; Ratner, M. A.; Marks, T. J. *J. Am. Chem. Soc.* **2009**, *131*, 11080.
(39) Lee, B. H.; Ryu, M. K.; Choi, S. Y.; Lee, K. H.; Im, S.; Sung, M. M. *J. Am. Chem. Soc.* **2007**, *129*, 16034.
(40) Tredgold, R. H. *Nature* **1991**, *354*, 120.
(41) Ulman, A. *Chem. Rev.* **1996**, *96*, 1533.
(42) Lee, H.; Kepley, L. J.; Hong, H. G.; Akhter, S.; Mallouk, T. E. *J. Phys. Chem.* **1988**, *92*, 2597.
(43) Lee, H.; Kepley, L. J.; Hong, H. G.; Mallouk, T. E. *J. Am. Chem. Soc.* **1988**, *110*, 618.

(44) Katz, H. E.; Scheller, G.; Putvinski, T. M.; Schilling, M. L.; Wilson, W. L.; Chidsey, C. E. D. *Science* **1991**, *254*, 1485.
(45) Katz, H. E.; Schilling, M. L. *Chem. Mater.* **1993**, *5*, 1162.
(46) Ha, Y. G.; Facchetti, A.; Marks, T. J. *Chem. Mater.* **2009**, *21*, 1173.
(47) Lin, W. B.; Lin, W. P.; Wong, G. K.; Marks, T. J. *J. Am. Chem. Soc.* **1996**, *118*, 8034.
(48) Zhu, P. W.; van der Boom, M. E.; Kang, H.; Evmenenko, G.; Dutta, P.; Marks, T. J. *Chem. Mater.* **2002**, *14*, 4982.
(49) Yoon, M. H.; Facchetti, A.; Marks, T. J. *Proc. Natl. Acad. Sci. U.S.A.* **2005**, *102*, 4678.
(50) Wang, L.; Yoon, M. H.; Lu, G.; Yang, Y.; Facchetti, A.; Marks, T. J. *Nat. Mater.* **2006**, *5*, 893.
(51) Facchetti, A.; Abbotto, A.; Beverina, L.; van der Boom, M. E.; Dutta, P.; Evmenenko, G.; Pagani, G. A.; Marks, T. J. *Chem. Mater.* **2003**, *15*, 1064.
(52) Kim, C.; Facchetti, A.; Marks, T. J. *Science* **2007**, *318*, 76.
(53) Parratt, L. G. *Phys. Rev.* **1954**, *95*, 359.
(54) Nelson, A. *J. Appl. Crystallogr.* **2006**, *39*, 273.
(55) Malik, A.; Lin, W.; Durbin, M. K.; Marks, T. J.; Dutta, P. *J. Chem. Phys.* **1997**, *107*, 645.
(56) Fukuto, M.; Heilmann, R. K.; Pershan, P. S.; Yu, S. J. M.; Soto, C. M.; Tirrell, D. A. *J. Chem. Phys.* **2003**, *119*, 6253.
(57) Lin, W. B.; Lee, T. L.; Lyman, P. F.; Lee, J. J.; Bedzyk, M. J.; Marks, T. J. *J. Am. Chem. Soc.* **1997**, *119*, 2205.
(58) Ha, Y. G.; Jeong, S.; Wu, J. S.; Kim, M. G.; Dravid, V. P.; Facchetti, A.; Marks, T. J. *J. Am. Chem. Soc.* **2010**, *132*, 17426.
(59) Byrne, P. D.; Facchetti, A.; Marks, T. J. *Adv. Mater.* **2008**, *20*, 2319.
(60) Kim, C.; Facchetti, A.; Marks, T. J. *Adv. Mater.* **2007**, *19*, 2561.
(61) Jeong, S.; Jeong, Y.; Moon, J. *J. Phys. Chem. C* **2008**, *112*, 11082.
(62) Kim, D.; Jeong, Y.; Song, K.; Park, S. K.; Cao, G. Z.; Moon, J. *Langmuir* **2009**, *25*, 11149.
(63) Seo, S. J.; Hwang, Y. H.; Bae, B. S. *Electrochem. Solid-State Lett.* **2010**, *13*, H357.
(64) Chua, L. L.; Zaumseil, J.; Chang, J. F.; Ou, E. C. W.; Ho, P. K. H.; Sirringhaus, H.; Friend, R. H. *Nature* **2005**, *434*, 194.
(65) Hulea, I. N.; Fratini, S.; Xie, H.; Mulder, C. L.; Iossad, N. N.; Rastelli, G.; Ciuchi, S.; Morpurgo, A. F. *Nat. Mater.* **2006**, *5*, 982.
(66) Yoon, M. H.; Kim, C.; Facchetti, A.; Marks, T. J. *J. Am. Chem. Soc.* **2006**, *128*, 12851.
(67) Jo, S. J.; Kim, C. S.; Kim, J. B.; Kim, J.; Lee, M. J.; Hwang, H. S.; Baik, H. K.; Kim, Y. S. *Appl. Phys. Lett.* **2008**, 93.
(68) Hwang, D. K.; Lee, K.; Kim, J. H.; Im, S.; Kim, C. S.; Baik, H. K.; Park, J. H.; Kim, E. *Appl. Phys. Lett.* **2006**, 88.
(69) Zirkl, M.; Haase, A.; Fian, A.; Schon, H.; Sommer, C.; Jakopic, G.; Leising, G.; Stadlober, B.; Graz, I.; Gaar, N.; Schwodiauer, R.; Bauer-Gogonea, S.; Bauer, S. *Adv. Mater.* **2007**, *19*, 2241.
(70) Whitesides, G. M.; Grzybowski, B. *Science* **2002**, *295*, 2418.
(71) Love, J. C.; Estroff, L. A.; Kriebel, J. K.; Nuzzo, R. G.; Whitesides, G. M. *Chem. Rev.* **2005**, *105*, 1103.
(72) Action, B. O.; Ting, G. G.; Shamberger, P. J.; Ohuchi, F. S.; Ma, H.; Jen, A. K. Y. *ACS Appl. Mater. Interfaces* **2010**, *2*, 511.
(73) Fukuda, K.; Hamamoto, T.; Yokota, T.; Sekitani, T.; Zschieschang, U.; Klauk, H.; Someya, T. *Appl. Phys. Lett.* **2009**, 95.
(74) Brzoska, J. B.; Shahidzadeh, N.; Rondelez, F. *Nature* **1992**, *360*, 719.
(75) Tao, Y. T. *J. Am. Chem. Soc.* **1993**, *115*, 4350.
(76) Spori, D. M.; Venkataraman, N. V.; Tosatti, S. G. P.; Durmaz, F.; Spencer, N. D.; Zurcher, S. *Langmuir* **2007**, *23*, 8053.
(77) Boulas, C.; Davidovits, J. V.; Rondelez, F.; Vuillaume, D. *Phys. Rev. Lett.* **1996**, *76*, 4797.
(78) Virkar, A. A.; Mannsfeld, S.; Bao, Z. A.; Stingelin, N. *Adv. Mater.* **2010**, *22*, 3857.
(79) Yang, S. Y.; Shin, K.; Park, C. E. *Adv. Funct. Mater.* **2005**, *15*, 1806.
(80) Kobayashi, S.; Nishikawa, T.; Takenobu, T.; Mori, S.; Shimoda, T.; Mitani, T.; Shimotani, H.; Yoshimoto, N.; Ogawa, S.; Iwasa, Y. *Nat. Mater.* **2004**, *3*, 317.
(81) Rivnay, J.; Jimison, L. H.; Northrup, J. E.; Toney, M. F.; Noriega, R.; Lu, S. F.; Marks, T. J.; Facchetti, A.; Salleo, A. *Nat. Mater.* **2009**, *8*, 952.
(82) Fritz, S. E.; Kelley, T. W.; Frisbie, C. D. *J. Phys. Chem. B* **2005**, *109*, 10574.
(83) Steudel, S.; De Vusser, S.; De Jonge, S.; Janssen, D.; Verlaak, S.; Genoe, J.; Heremans, P. *Appl. Phys. Lett.* **2004**, *85*, 4400.
(84) Knipp, D.; Street, R. A.; Volkel, A. R. *Appl. Phys. Lett.* **2003**, *82*, 3907.
(85) Pernstich, K. P.; Haas, S.; Oberhoff, D.; Goldmann, C.; Gundlach, D. J.; Batlogg, B.; Rashid, A. N.; Schitter, G. *J. Appl. Phys.* **2004**, *96*, 6431.